ORIGINAL PAPER

The Impact of Shear Rate on the Mechanical Behavior of Rock Joints Under Multiple-Influencing Factors

Liu He[1] · Xudong Lu[1] · Tim Copeland[2] · Jiannan Chen[2] · Jiaxin Yan[1] · Wang Zhao[1]

Abstract

The shear rate is an important factor that influences the shear mechanical properties of rock joints. In this paper, constant normal load (CNL) direct shear tests at different shear rates (v_s = 0.2–5.0 mm/min) were performed on rock joint specimens to investigate the shear behavior and failure modes under various joint roughness coefficients (JRC = 6.071–17.212), joint wall compressive strengths (JCS = 9.36–25.86 MPa), and normal stresses (σ_n = 0.936–2.586 MPa). The experimental results indicated that the peak shear strength gradually decreased, the peak shear displacement increased and the residual shear strength decreased with increasing shear rate. The experimental findings suggested that with an increasing JRC and a decreasing JCS and σ_n, the peak shear strength and peak shear displacement were greatly influenced by the shear rate. Additionally, shear-off and wear failure modes were observed in this research and were both intensified by increasing shear rates. However, the failure mode tended to change from wear to shear-off as the shear rate increased, and this phenomenon was enhanced when JRC, JCS, and σ_n decreased. A modified new shear strength correlation model that related v_s and valid values of JRC, JCS, and σ_n was developed to estimate the shear strength of rock joints. The predicted results indicated that the newly proposed model performed better than the existing models.

Keywords Rock joint · Shear rate · Mechanical behavior · Failure mode · Shear strength criterion

Highlights

- The influence of the shear rate on the valid values of joint roughness coefficients, joint wall compressive strengths, and normal stresses was evaluated.
- The evolution of the mechanical behavior and failure modes of rock joints related to the shear rate was investigated.
- A shear strength correlation model that related to shear rate was proposed to estimate the shear strength of rock joints.

✉ Liu He
heliu@home.swjtu.edu.cn

1 Faculty of Geosciences and Environmental Engineering, Southwest Jiaotong University, No. 999 On Road Xi-an, Xipu Town, Pixian County, Chengdu 611756, Sichuan, People's Republic of China

2 Department of Civil, Environmental, and Construction Engineering, University of Central Florida, Orlando, FL, USA

1 Introduction

Rock joints, such as bedding, faults, and fractures, are the most extensive and complex discontinuities in a rock mass. The shear behavior of rock joints is an important measure of the rock mass in the evaluation of slope stability, foundation, and underground excavations. Currently, most constitutive models that describe the rock joint shear behavior consider the joint surface morphology, joint wall material properties, and applied normal stress (Barton and Choubey 1977; Plesha 1987; Jing 1990; Amadei and Saeb 1990; Wibowo 1994; Zhao 1997a, b; Amadei et al. 1998; Grasselli and Egger 2003; Xia et al. 2014). However, several studies have confirmed that various shear rate (v_s) circumstances are induced by the creep deformation of rock masses, earthquakes, and blasts, which is a critical factor affecting the mechanical behavior of rock joints (Wang and Konietzky 2009; Meng et al. 2019). Thus, the behavior of rock joints under different shear rates has received extensive attention in the last few years.

It has been generally recognized that the peak shear strength of rock joints decreases with increasing shear rates (Barbero et al. 1996; Jafari et al. 2003; Atapour and Moosavi 2014; Tang et al. 2015). However, it is also found that the mechanical behavior of rock joints, based on various parameters, will be significantly different under the influence of shear rate. For example, Crawford and Curran (1981) found that for joints in granite with intermediate hardness, the frictional resistance was essentially independent of the shear rate, while for the hardest rocks, the syenite and sandstone rock joints showed a significant variation in shear resistance with shear rate. Tiwari and Latha (2019) believed that although the shear strength of discontinuities decreases with increasing shear rate, decreasing rock density enhances this rate dependency of rock joint strength. Wang et al. (2020) observed that as the shear rate increases from 0.001 to 0.1 mm/s, the cohesion increases by 5.8% when the JRC is 19 and increases by 1.9% when the JRC is 1, which illustrates that joints with greater asperity roughness values exhibit a stronger shear rate dependency. Therefore, to accurately determine the joint shear strength under different shear rates, it is necessary to consider the influence of rock joint parameters.

In recent years, a few studies categorized the failure modes of joints as sliding, wear, shear-off, climbing failure, and gnawing (Li 2017; Li et al. 2019; Kou et al. 2019), but these works did not further analyze the interaction of failure mode evolution with shear rate. Since the acoustic emission (AE) monitoring technique can effectively identify the location and magnitude of failure during the shear process, the AE characteristics of joints under different shear rates have been studied by some scholars (Zhou et al. 2016; Wang et al. 2016; Meng et al. 2019), and it is found that the curves of the AE count and AE energy rate illustrate that cracks in the rock joints occur earlier under a larger shear rate. In addition, under cyclic loading at different shear rates, it was found that as the normal stress increased, the effect of the shear rate became less pronounced for rock joints (Jafari et al. 2004; Mirzaghorbanali et al. 2014), but for an infilled joint under cyclic loading tests, the failure modes under different shear rates seem to be identical (Han et al. 2020).

Although previous researchers have analyzed the shear rate on the shear strength and failure mode of rock joints, the diverse shear rate effect of the joint under different mechanical parameters has not yet been systematically studied. Additionally, constitutive models are fundamental for numerical modeling and theoretical calculations in rock joint engineering. Over the last few decades, several constitutive models have been formulated to simulate the shear behavior of rock joints (Patton 1966; Ladanyi and Archambault 1969; Barton and Choubey 1977; Plesha 1987; Wibowo 1994; Zhao 1997a, b; Amadei et al. 1998; Grasselli and Egger 2003;

Xia et al. 2014; Tang and Wong 2016; Saadat et al. 2021). However, these constitutive models do not involve the shear rate and cannot adequately predict the shear strength under various shear rates.

In this study, a series of constant normal load (CNL) direct shear tests for rock joint specimens were carried out under multiple values of the joint roughness coefficient (JRC), joint wall compressive strength (JCS), normal stress (σ_n), and shear rate (v_s). The evolution of the mechanical behavior and failure modes of rock joints related to the shear rate was further investigated. Additionally, the influence of the shear rate on valid values of JRC, JCS, and σ_n was evaluated, and a modified empirical criterion that considers the shear rate was developed for engineering practice.

2 Materials and Methods

2.1 Specimen Preparation

Discontinuities in natural rocks are extremely complicated and varied, and it is difficult to obtain a series of joints with the same morphology from a natural rock mass. Therefore, in this study, artificial rock materials and 3D printing technology were applied to fabricate a series of artificial joint specimens with similar surface morphologies.

Four artificial rock materials were produced by mixing quartz sand, cement, gypsum, and water using four different proportion designs. The uniaxial compressive strength test following the ASTM standards was carried out to determine the artificial rock material strength (Fig. 1a). The basic mechanical properties of the four artificial rock materials, including density, Young's modulus and uniaxial compressive strength (UCS), are shown in Table 1. Barton recommended that for intact and unweathered rock joints, the JCS is equivalent to the UCS. Therefore, the JCS values in this research were set the same as the UCS values. As shown in Fig. 1, the specimen preparation process is described as follows:

1) Four standard roughness profiles (NO. 4, NO. 6, NO. 8, and NO. 10) suggested by Barton and Choubey (1977) were selected as the specimen representative surface morphology, which were scanned with a high-precision scanner (Epson DS-30000) and then digitized through the OriginPro Program 2017 software package. Four plastic sheets with different JRC profiles were produced through a 3D printing program (Fig. 1b);

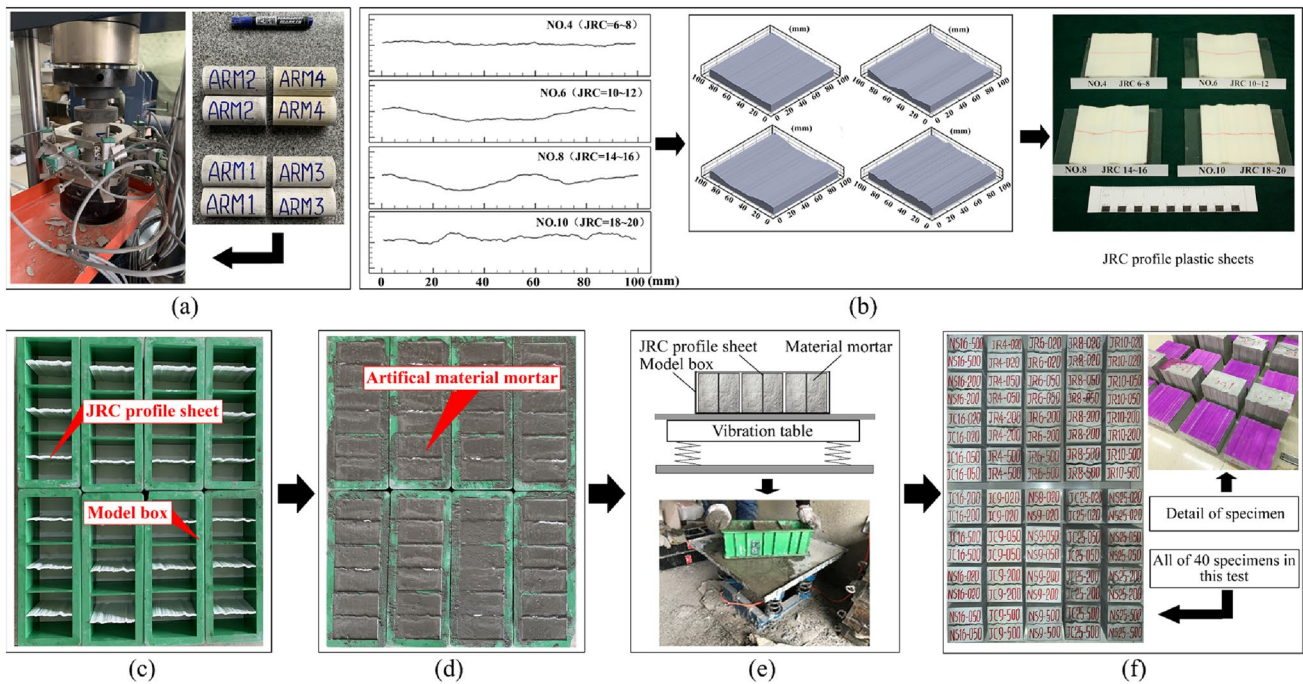2) The JRC sheet was placed in a 100 mm * 100 mm * 100 mm cubic model box (Fig. 1c);

Fig. 1 The specimen preparation process: **a** cylindrical uniaxial compressive strength test for artificial rock materials, **b** digitizing the standard JRC profiles and JRC plastic sheets produced by 3D printing technology, **c** the JRC sheet was placed in a cubic model box, **d** mortar was poured into the cubic box, **e** the cubic box was placed on a vibration table to remove the air bubbles in the mixed mortar, and **f** rock joint specimens after curing

Table 1 The basic mechanical properties of the artificial rock materials

Artificial rock materials	Density (g/cm^3)	Young's modulus (GPa)	UCS (MPa)
ARM1	1.94	2.75	9.36
ARM2	2.19	4.58	16.42
ARM3	2.25	6.04	19.49
ARM4	2.39	7.61	25.86

3) The artificial rock aggregates were poured into a blender and stirred, and then the mortar was poured into the cubic box (Fig. 1d);

4) After each addition of mortar, the cubic box was placed on a vibration table to remove air bubbles in the mixed mortar (Fig. 1e);

5) Since concrete materials require 28 days of curing to reach their ultimate strength (ASTM C150, 2005), the specimens were demolded after 24 h and cured in an indoor environment for more than 40 days until they reached their ultimate strength. A total of 40 specimens with different properties were cast with joint surface dimensions of 100 mm*100 mm. Both the upper and lower surfaces of the specimen shear surfaces were colored pink for better visibility of the damage and characteristics after shearing (Fig. 1f).

2.2 Quantitative Description of the Joint Surface Morphology

During the past few decades, the JRC has been the most commonly used parameter to quantitatively describe the roughness of rock discontinuities in various constitutive models. Tse and Cruden (1979) found that the dimensionless first derivative root mean square Z_2 statistical parameter (Eq. 1) had the highest correlation with the JRC. Therefore, this paper employed the correlation equation proposed by Tse and Cruden (Eq. 2) for the relationship between the JRC and Z_2 for quantitative joint morphology and used it to calculate the JRC value. The calculation parameters of Z_2 are shown in Fig. 2.

$$Z_2 = \left[\frac{1}{L} \int_{x=0}^{x=L} \left(\frac{dy}{dx} \right)^2 dx \right]^{1/2} = \left[\frac{1}{L} \sum_{i=1}^{n-1} \frac{(y_{i+1} - y_i)^2}{x_{i+1} - x_i} \right]^{1/2},$$
(1)

$$JRC = 32.2 + 32.47 \log Z_2.$$
(2)

In this test, an HP Pro S3 3D image capture system was used to scan and calculate the Z_2 value of each joint

Fig. 2 Diagram used to define the statistical parameters for a joint profile. Here, y_i is the height of a joint profile at x_i, and $\triangle x$ is the distance between x_{i+1} and x_i, which is set as 0.5 mm in this research. L is the horizontal length of a joint profile (Kulatilake et al. 1995)
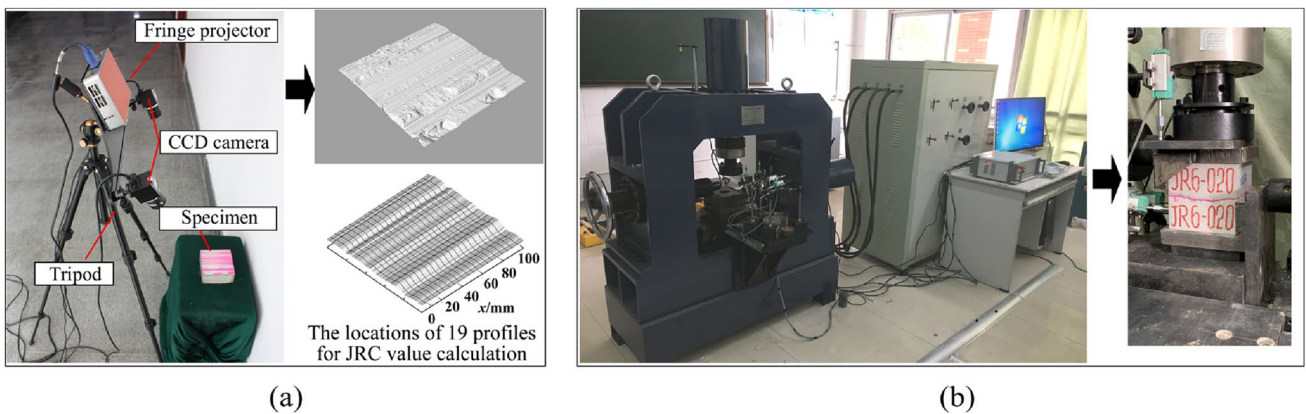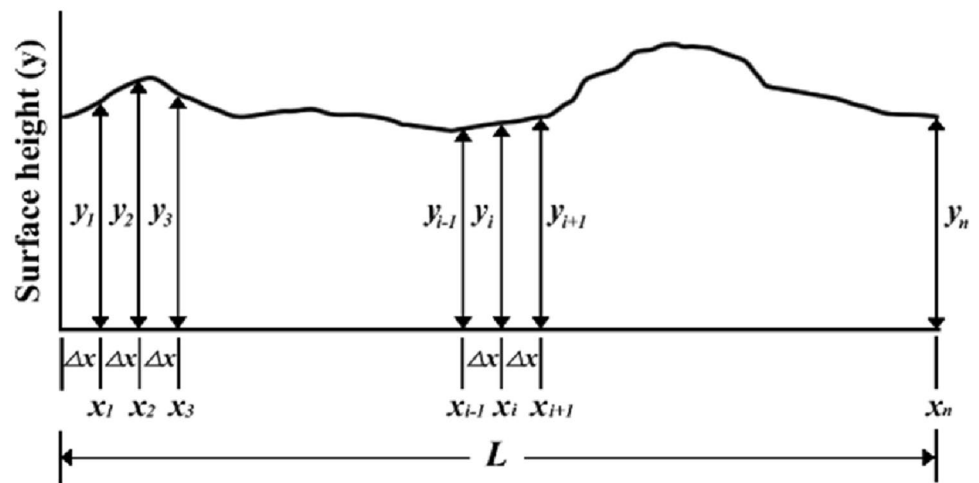

Fig. 3 The test apparatus used in this study: **a** joint surface asperity capture system and the 19 profile locations used for data analysis, **b** the CNL servo control direct shear test apparatus

Table 2 Test programs and mechanical properties of the specimens

Test group	JRC	JCS (MPa)	σ_n (MPa)	K = JCS/σ_n	Shear rate (mm/min)			
JR04	6.071	19.49	1.949	10.000	0.2	0.5	2.0	5.0
JR06	10.270	19.49	1.949	10.000				
JR08	13.898	19.49	1.949	10.000				
JR10 or JC19 or NS19	17.212	19.49	1.949	10.000				
JC09	17.212	9.36	1.949	4.802				
JC16	17.212	16.42	1.949	8.425				
JC25	17.212	25.86	1.949	13.268				
NS09	17.212	9.36	0.936	10.000				
NS16	17.212	16.42	1.642	10.000				
NS25	17.212	25.86	2.586	10.000				

specimen surface profile. The system included a measuring head and a modeling program (Fig. 3a). The measuring head consisted of a fringe projector and two CCD cameras. During the capture of an image, the 3D capture system projected a raster picture onto the joint surface, and the picture was recorded by the cameras. The modeling program was used to accurately analyze the spatial coordinates of each point on the surface of the scanned object and complete the 3D modeling of the object. The capture system used in this experiment had a single scan time of 2–4 s, a single scan size of 60–500 mm, and a scanning precision of 0.06 mm. To efficiently limit the calculation

error of the JRC, 19 profiles were selected on the upper and lower surfaces at a spacing of 5.0 mm along the shear direction (Fig. 3a), and the average JRC value for 38 profiles was obtained for further analysis. The initial JRC values calculated for each specimen by Eqs. (1) and (2) are listed in Table 2.

2.3 Test Apparatus and Process

The CNL automated servo control direct shear test apparatus used in this study had a maximum stress of 500 kN in the normal and shear directions and a maximum horizontal displacement of 200 mm (Fig. 3b). As discussed above, the four variables set in this test were as follows: the JRC values were set to 6.071, 10.270, 13.898, and 17.212; the JCS values were selected as 9.36, 16.42, 19.49, and 25.86 MPa; and four levels of normal stress (0.936, 1.642, 1.949, 2.586 MPa) were set. Moreover, the test was conducted at four shear rates: 0.2, 0.5, 2.0, and 5.0 mm/min. The experimental programs are shown in Table 2. To facilitate analysis of the test results, the joint strength coefficient ($K = JCS/\sigma_n$) is introduced in the subsequent discussion.

During testing, when the shear displacement δ reached the preset value (in this test, shear displacement = 0.1*length of joint shear direction = 10 mm), the test was halted. The loose debris caused by joint surface damage was removed with a soft brush, and then the joint surface morphology was captured again by the 3D image capture system.

3 Results and Discussion

3.1 Shear Strength Versus Shear Displacement Curves

The shear strength as a function of shear displacement under various shear rates is shown in Fig. 4. All curves demonstrate obvious pre-peak, peak, and post-peak strength phases. Taking specimen JR10/JC19/NS19 as an example (Fig. 4j), as the shear rate increases from 0.2 to 5.0 mm/min, the peak shear displacement gradually increases from 1.839 to 2.289 mm, while the peak shear strength decreases from 2.959 to 2.677 MPa. The shear rate was found to be positively correlated with the peak shear displacement and negatively correlated with the peak shear strength, which is consistent with the observations from previous studies (Tang and Wong 2016; Meng et al. 2019; Wang et al. 2016). These observations can then be interpreted as follows: as the shear rate increases, the joint interface has insufficient time to generate adequate contact and frictional resistance during shearing. Therefore, the actual contact area at the asperity contact points decreases, resulting in higher peak shear displacement and lower peak shear strength. After the curves

entered the post-peak phase, the shear strength continued to decrease and was finally maintained near the residual shear strength. The residual shear strength decreased from 2.469 to 2.003 MPa with a shear rate from 0.2 to 5.0 mm/min in specimen JR10/JC19/NS19.

3.2 Effects of Multiple Factors on Peak Shear Strength and Peak Shear Displacement

To further study the effect of the shear rate on the peak shear strength and peak shear displacement under multiple influencing factors, the variation rate of the peak shear strength and peak shear displacement was calculated. The variation rate of peak shear strength and peak shear displacement is defined as the ratio of the peak shear strength and peak shear displacement obtained under various shear rates (0.2, 0.5, 2.0, 5.0 mm/min) to the peak shear strength and peak shear displacement obtained using a shear rate of 0.2 mm/min, respectively. Figures 5 and 6 show the variation rates of the peak shear strength and peak shear displacement with the shear rate for different JRC, JCS, and σ_n values.

The variation rates of the peak shear strength and peak shear displacement under the different JRCs are plotted in Figs. 5a and 6a, respectively. As the shear rate increased from 0.2 to 5.0 mm/min, it was revealed that the variation rate of the peak shear strength and peak shear displacement tended to enhance with increasing JRC, which confirmed that the joints with greater roughness were more sensitive to the effect of the shear rate change.

Figures 5b and 6b show the variation rates of the peak shear strength and peak shear displacement under different JCSs. Due to the relatively weak strength of the joint wall material in specimen JC09 in comparison to the other specimens, as the shear rate increased, the wear and fracture damage of the joint wall materials were more easily enhanced, which caused shear mechanical and deformation properties of the joint that were more influenced by the shear rate increase. Conversely, the joint wall material with higher strength has a greater capacity to resist wear and damage, which means that the variation rate of peak shear strength and peak shear displacement is less affected by the shear rate change.

Figures 5c and 6c demonstrate the variation rate of the peak shear strength and peak shear displacement with different σ_n. Due to the lower normal stress boundary conditions for specimen NS09, the friction resistance generated by the joint interface was smaller, and the relative slip in the horizontal direction and dilation in the vertical direction easily occurred under various shear rates, which caused the shear mechanical parameters to easily change over a wide range with increasing shear rates. In contrast, as σ_n increased, the interfacial friction increased, and the influence of the shear rate on the joint shear mechanical parameters tended
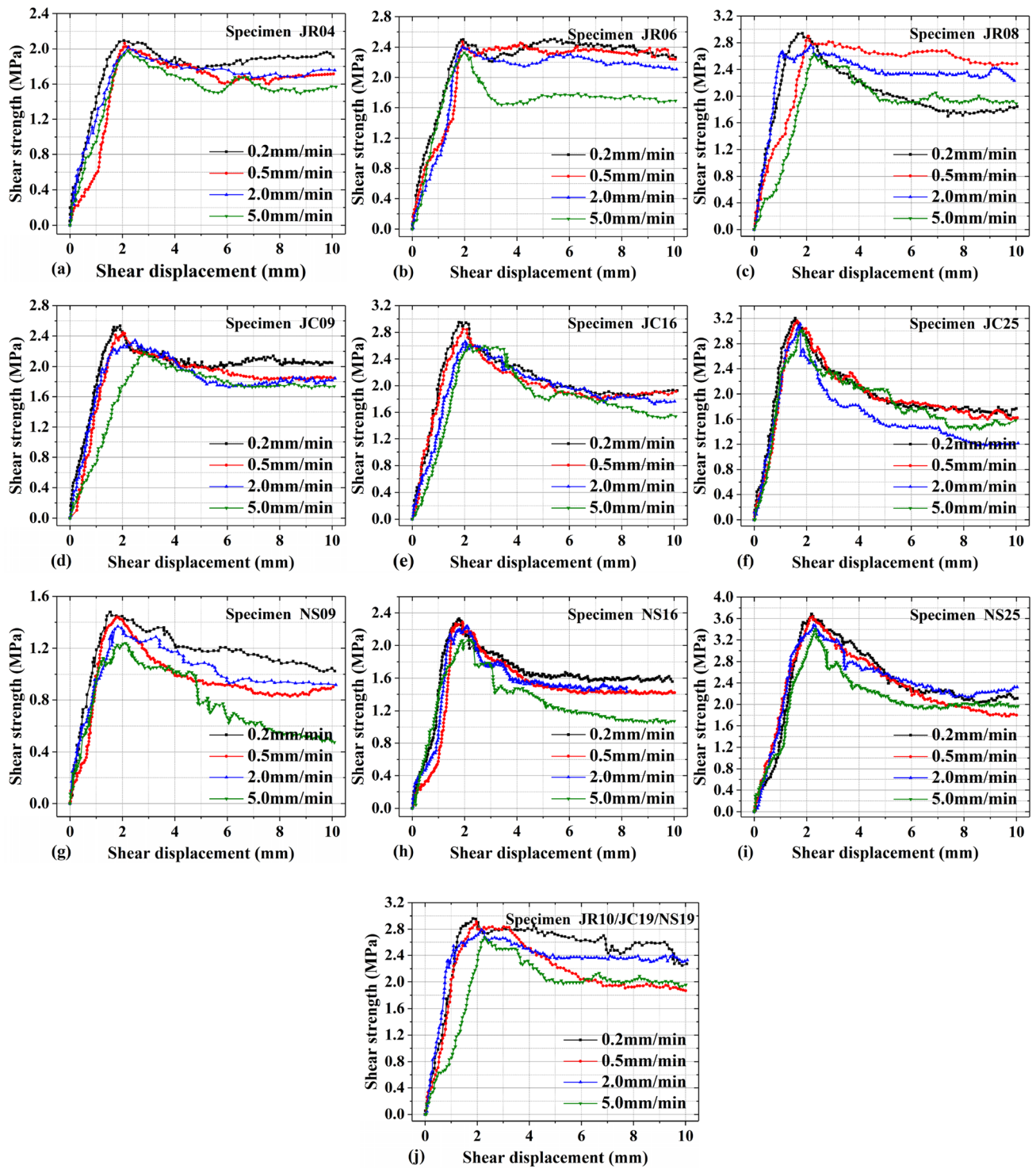
Fig. 4 The shear strength versus shear displacement curves for various specimens
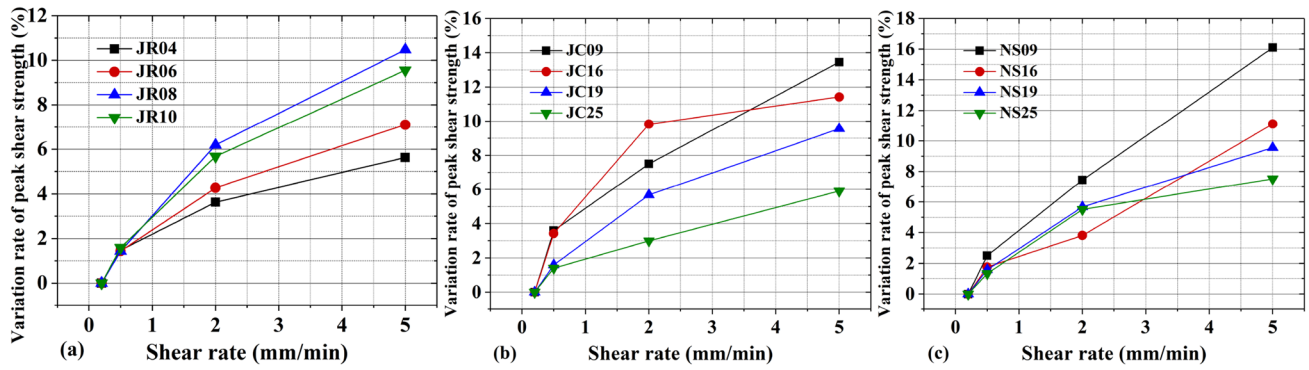
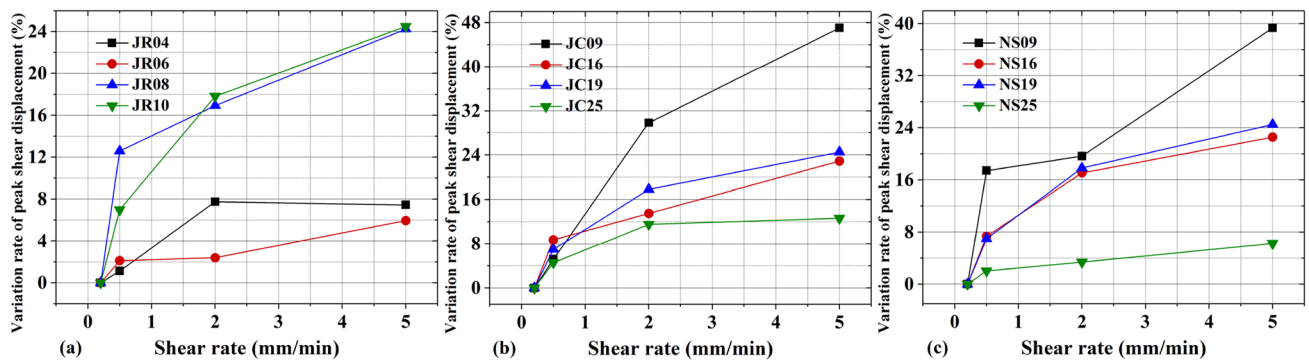**Fig. 5** Effect of shear rate on the variation rate of the peak shear strength for various specimens

Fig. 6 Effect of shear rate on the variation rate of the peak shear displacement for various specimens
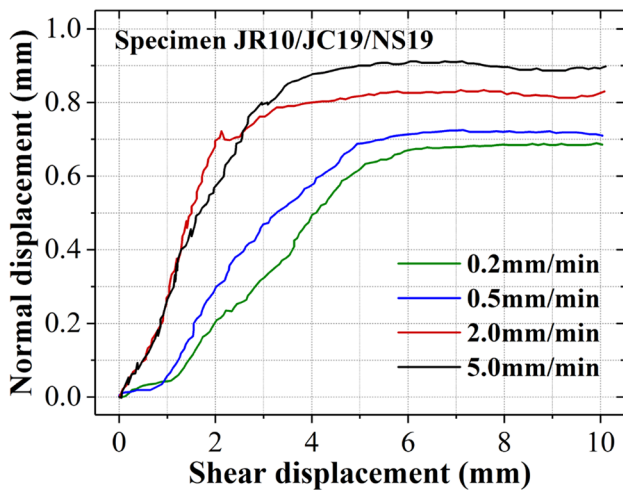

Fig. 7 Normal and shear displacement curves of a joint at different shear rates

to weaken. Therefore, the joint shear mechanical properties of the specimen with higher σ_n were less affected by the shear rate.

3.3 Normal Displacement Versus Shear Displacement Curves

Figure 7 shows the normal displacement versus shear displacement curves of specimen JR10/JC19/NS19. It was observed that the curve with a shear rate of 0.2 mm/min comprises three obvious stages: slow growth, rapid growth, and stability. When the shear displacement is less than 1.2 mm, the curve exhibits a slow upward trend. Subsequently, with the shear displacement varying from 1.2 to 6.0 mm, the normal displacement increases rapidly and then reaches a constant value after the shear displacement exceeds 6.0 mm. For the curve with a shear rate of 0.5 mm/min, the curve shows three stages similar to that of 0.2 mm/min, but a smaller critical shear displacement value of the three-stage transition was observed. In contrast, for the curves with shear rates of 2.0 and 5.0 mm/min, the curves do not exhibit an obvious slow growth stage, but they immediately enter the rapid growth stage at the beginning of the test. Meanwhile, as the shear displacement increased, the normal displacement also promptly increased until the curve reached the stability stage. Therefore, with the increase in shear rate from 0.2
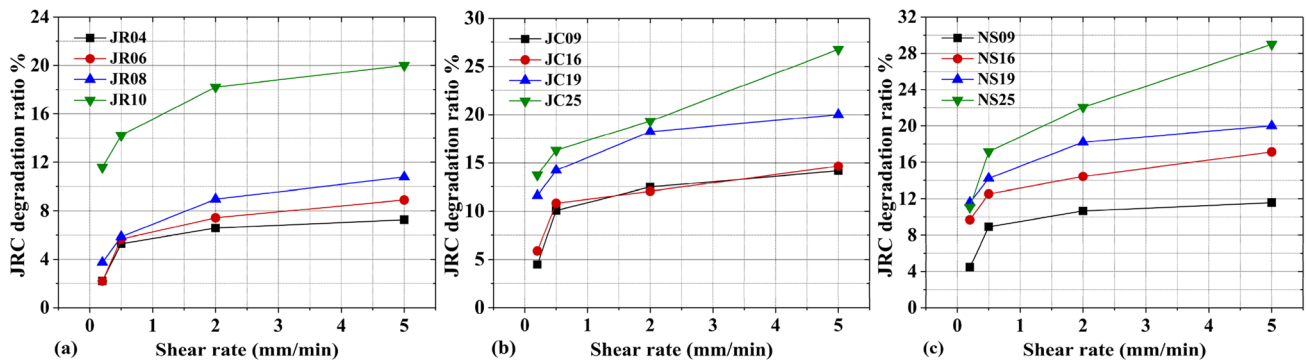
Fig. 8 Effect of shear rate on the JRC degradation ratio for various specimens

to 5.0 mm/min, the curve exhibited a trend from three stages to two stages, and the peak normal displacement was enhanced from 0.684 to 0.892 mm at shear rates from 0.2 to 5.0 mm/min.

3.4 Effect of Multiple Factors on Joint Failure Characteristics

Based on the experimental observations of the joint asperity surface failure characteristics after the test, this section attempts to explore the joint failure characteristics and modes of joints under multiple influencing factors.

3.4.1 Effect of Multiple Factors on Asperity Roughness Degradation

Figure 8 illustrates the JRC degradation ratio of the specimens with respect to the shear rate after the test. The JRC degradation ratio is defined as the ratio of the JRC variation to the initial JRC: [(JRC$_{initial}$–JRC$_{after}$)/JRC$_{initial}$]*100%. In general, the JRC degradation ratio nonlinearly increased as the shear rate increased. It is revealed that various JRC, JCS, and σ_n values also had a significantly different effect on the asperity degradation behavior under distinct shear rate conditions.

As shown in Fig. 8a, as the shear rate increased from 0.2 to 5.0 mm/min, the JRC degradation ratio increased by 5.03%, 6.07%, 7.04%, and 8.42% for specimens JR4, JR6, JR8, and JR10, respectively. This result indicates that the asperity degradation of the rough joint surface is more easily affected by the shear rate compared to the smooth joint surface. Analyzing the reason for this phenomenon, we believe that for rock joint specimens with the same geometry, a larger roughness coefficient represents a larger contact area between the upper and lower sections of the asperity surface, resulting in greater surface damage during shear. Changing the shear rate will have a significant effect on the contact time of the shear surface, which will

make the joint surface with a rougher morphology more subject to the effect of the shear rate.

Figure 8b shows the JRC degradation ratio as a function of shear rate at different JCSs. For the rock joint specimens with larger JCS values, the convex area of the joint surface tends to exhibit brittle failure, which results in crack initiation and rapid propagation occurring in the convex body and failure of the joint surface over a wide area. This phenomenon becomes more pronounced as the shear rate increases. In addition, as the shear rate increased from 0.2 to 5.0 mm/min, the JRC degradation ratio of specimen JC25 increased by 13.1%, while that of specimen JC09 increased by 9.7%. This suggests that with increasing JCS value, roughness degradation was more sensitive to shear rate.

Higher normal stress can significantly increase the potential contact area between the joint surface, which enhances the roughness degradation in the shearing process. As demonstrated in Fig. 8c, with increasing σ_n, the joint roughness degradation intensified at a specific shear rate. As the shear rate increased from 0.2 to 5.0 mm/min, the JRC degradation ratio increased by 7.1% for NS09, 7.5% for NS16, 8.4% for NS19, and 17.9% for NS25. Clearly, with increasing σ_n, the shear rate was more critical to joint degradation.

3.4.2 Failure Mode of the Joint Under Multiple Factors

In this test, the upper and lower sections of the asperity surface showed a similar failure mode. Pictures of the joint surface lower section failure after the test are shown in Fig. 9a. To quantitatively assess the damaged area for each specimen, the asperity surface pictures after the test were converted to binary images, as shown in Fig. 9b. The joint surface degradation coefficient, $\sum A_i/A_{joint}$, was used to represent the ratio of the total upper and lower surface damage area ($\sum A_i$) to the overall area of a joint specimen (A_{joint}) (Hong et al. 2016). The surface degradation coefficient for specimens
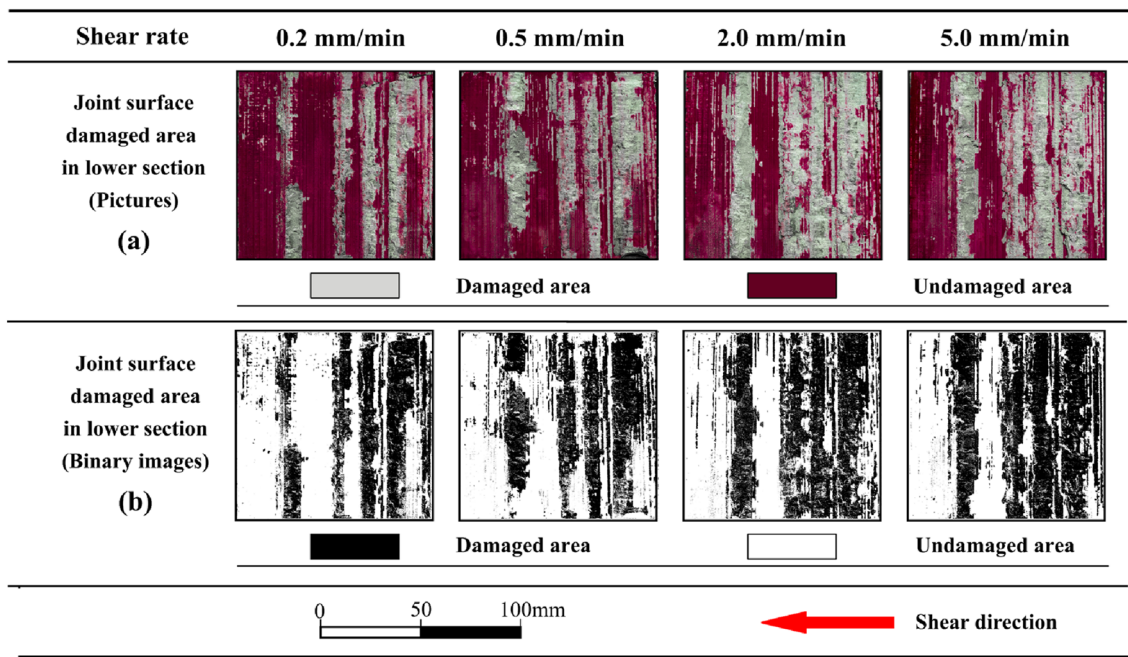
Fig. 9 Joint surface damage features under various shear rates: **a** joint surface damage pictures, **b** joint surface damage binary images
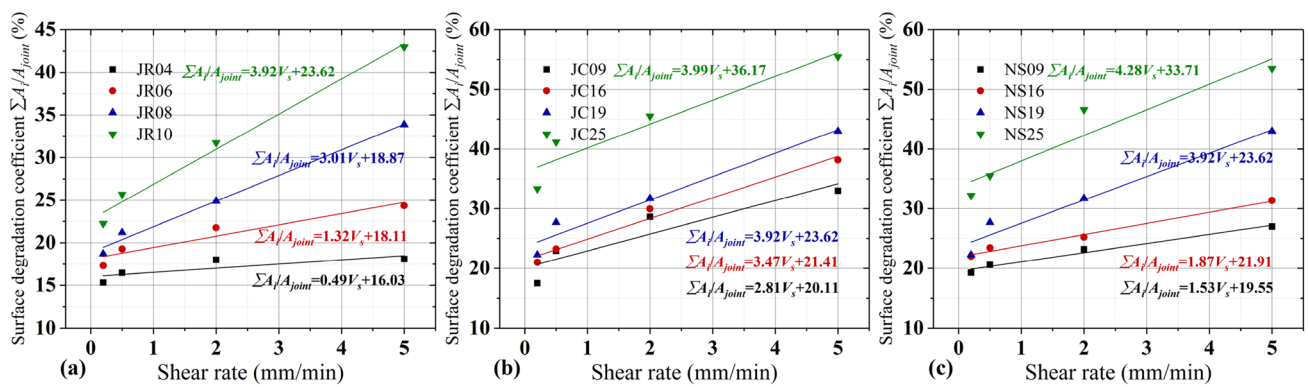

Fig. 10 The relationship between the joint surface asperity damage and the shear rate: joint surface degradation coefficient versus shear rate
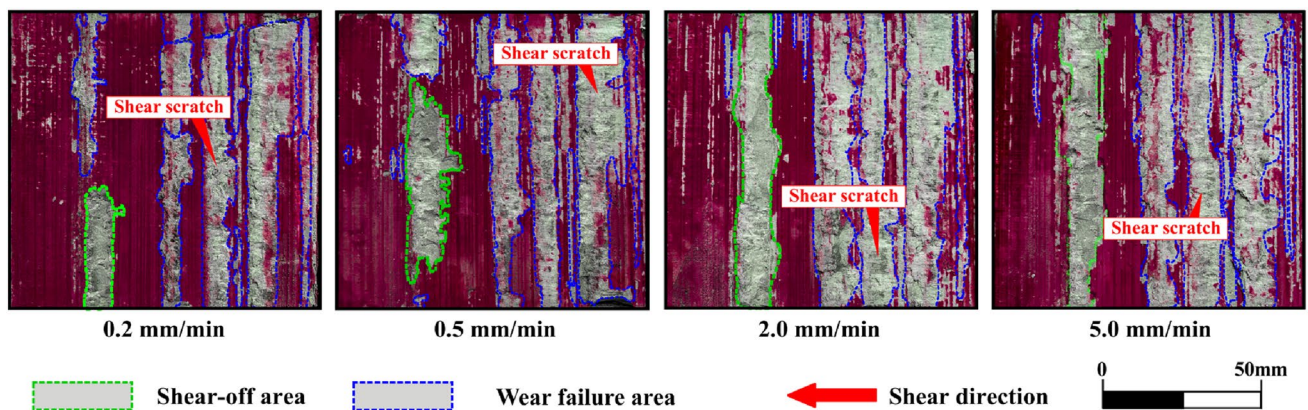

Fig. 11 Joint surface failure modes on the lower section of the joint surface

under various shear rates is shown in Fig. 10a, b, and c. In general, with the increase in shear rate, the degradation coefficient increases, and it presents an approximately linear relationship. The linear fitting of the test data (Fig. 10a, b, and c) reveals that the slope of the fitted line gradually increases with increases in JRC, JCS, and σ_n, such as in the cases of specimens JR04, JR06, JR08, and JR10, where the slope values of the fitted lines are 0.49, 1.32, 3.01, and 3.92 (Fig. 10a), respectively. This further proves that the sensitivity of asperity damage to the shear rate differed notably under various JRC, JCS, and σ_n conditions.

It has been experimentally demonstrated in previous research that joint failure processes exhibit various modes under multiple influencing factors (Huang et al. 2002, Asadi et al. 2012, Gui et al. 2019, Li 2017). In this test, shear-off and wear were the main failure modes observed (Fig. 11). Shear-off failure occurred mainly in the steep asperity areas, and shear fractures appeared along the shear direction, which led to a large range of damage to the joint surface convex body. Wear failure mainly occurred in the shallow contact area between the joint surface, and there were obvious sliding shear scratches along the shear direction of the joint surfaces. Notably, the shear rate changed the failure mode of the specimens under different JRC, JCS, and σ_n conditions.

According to the aforementioned description of shear-off and wear failure, the shear-off and wear failure areas on the joint upper and lower surfaces were identified and counted in each specimen after the test. As shown in Fig. 11, the green dotted line represents the shear-off failure area, and the blue dotted line represents the wear failure area. As the shear rate increased, both the shear-off and wear failure areas on the asperity surface increased to a certain extent. At the same time, some wear failure areas gradually transformed into shear-off failure with a shear rate. This may in part be explained by the fact that when the shear rate was extremely small, the upper and lower asperity surfaces had sufficient time to develop gradual contact and dilation during the shear process, which mainly led to wear failure. However, under

a large shear rate, rapid tension and shear damage were promoted in the steep asperity area, and large-scale clastic materials were generated. The failure of the joint surface was accompanied by shear-off failure and a noticeable sound during the shear process.

To discuss the evolution of the specimen failure mode with multiple factors, the ratio of the shear-off failure area ($\sum A_s$) to the total failure area ($\sum A_i$) is defined as the shear-off ratio, $\sum A_s / \sum A_i$. The curve of the shear-off ratio of the specimens with respect to the shear rate is shown in Fig. 12.

As shown in Fig. 12a, the specimens with higher roughness, such as JR10 and JR08, presented an obvious shear-off failure mode under different shear rates. However, for JR04 with less roughness, there was no shear-off failure found under a lower shear rate (0.2 mm/min and 0.5 mm/min), but when the shear rate gradually increased to 5.0 mm/min, the shear-off ratio increased from 0 to 19.19%. This result indicated that increasing the shear rate has the effect of promoting the failure mode transformation to shear-off, but this potential is more obvious in the specimen with less roughness.

Figure 12b shows the shear-off ratio versus shear rate for specimens with different JCS values. For specimens with higher JCS values, shear-off failure was more obvious in various shear rate tests. When the shear rate increased from 0.2 to 5.0 mm/min, the shear-off ratio increased by 13.42%, 13.96%, 10.01%, and 6.13% for JC09, JC16, JC19, and JC25, respectively, which proved that the failure modes of the specimens with lower JCS values were more prone to transformation.

As shown in Fig. 12c, shear-off failure under higher σ_n was more obvious at various shear rates. However, when the shear rate increased from 0.2 to 5.0 mm/min, the shear-off ratio of specimen NS09 with the lowest σ_n increased by 8.69%, while specimen NS25 with the highest σ_n increased by 5.27%, which indicates to some extent that the shear rate was more sensitive to the variation in the failure mode of the joint under lower σ_n.
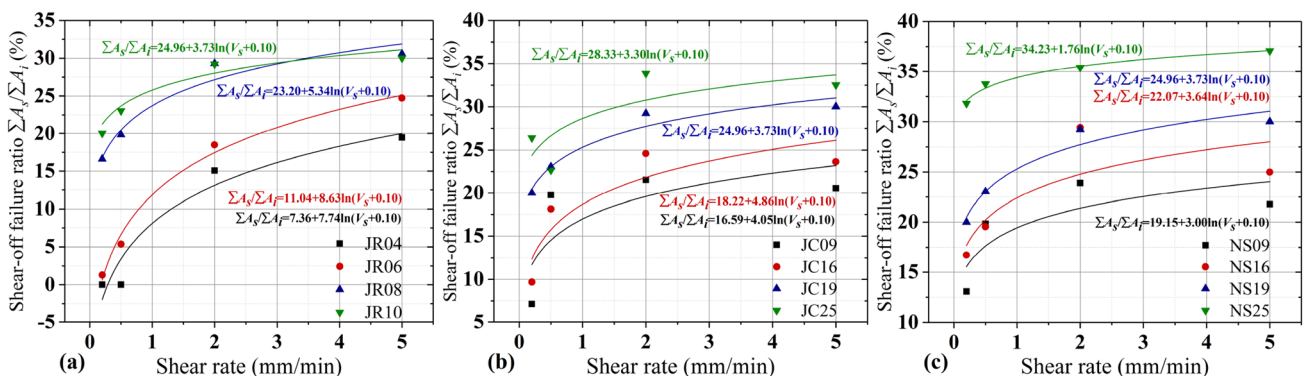

Fig. 12 The relationship between the joint surface asperity damage and the shear rate: shear-off failure ratio versus shear rate

Based on the above analysis, it can be concluded that with increasing shear rate, the failure mode of the rock joint tended to change from wear failure to shear-off failure. At the same time, for the specimens with larger JRC, JCS, and σ_n, the shear-off failure mode under different shear rates was more prominent, but considering the influence of the shear rate on the failure mode, the sensitivity of the failure mode converted by the shear rate was enhanced when JRC, JCS, and σ_n decreased.

4 Shear Strength Correlation Model

Barton's JRC–JCS model (Eq. 3) was one of the most widely used criteria for estimating the shear strength of rock joints due to its simplicity. However, this model did not consider the dependence of shear strength on shear rate and therefore did not explicitly give characteristics of shear behavior under varying shear rates. Recently, based on experimental results, Wang et al. (2016) proposed a model (Eq. 4) to predict the shear strength of rough rock joints under various shear rates.

$$\tau = \sigma_n \tan\left(JRC \log_{10} K + \phi_b\right), \tag{3}$$

$$\tau = 0.985 \sigma_n \tan\left[4.970(JRC)^{0.475} \log_{10} K + \phi_b\right] v_s^{-0.06}, \tag{4}$$

where σ_n, JRC and JCS are defined above, ϕ_b is the basic friction angle, K is the joint strength coefficient, $K = JCS/\sigma_n$, v_s is the shear rate, and τ is the shear strength.

However, the existing models remain insufficient to analyze the sensitivity of multiple influencing factors to shear strength. The study in Sect. 3 of this paper shows that the specimens with different values of JRC, JCS, and σ_n present different mechanical behaviors under various shear rates, and therefore, the valid values of JRC, JCS, and σ_n are changed to some extent under different shear rates. Consequently, it is reasonable to use the valid values of JRC, JCS, and σ_n under different shear rates in the mechanical strength evaluation of rock joints. In this section, based on Barton's JRC-JCS model and experimental results, a modified shear strength prediction model that considers the effects of shear rates on the JRC, JCS, and σ_n is proposed:

$$\tau = \left[\sigma_n(v_s) * \tan\left(JRC(v_s) * \log_{10} K(v_s) + \phi_b\right)\right] * f(v_s), \tag{5}$$

$$f(v_s) = G(v_s, \sigma_n, JRC, JCS), \tag{6}$$

where $\sigma_n(v_s)$, $JRC(v_s)$, and $K(v_s)$ are the valid normal stress, joint roughness coefficient, and joint strength coefficient, respectively, which are considered functions of the shear rate. $f(v_s)$ is a shear rate function related to multiple influencing factors (v_s, σ_n, JRC, and JCS).

Equation (5) shows that to obtain the modified shear strength, the undetermined coefficients that need to be obtained are $\sigma_n(v_s)$, $JRC(v_s)$, $K(v_s)$, and $f(v_s)$. Therefore, the following analysis was conducted:

(i) Considering only the influence of the JRC on the shear strength under different shear rates (such as specimens JR04, JR06, JR08, and JR10), the shear strength is shown in Eq. (7).

$$\tau = \left[\sigma_n \tan\left(JRC(v_s) * \log_{10} K + \phi_b\right)\right] * f(v_s)_{JRC,} \tag{7}$$

where $f(v_s)_{JRC}$ is a function related to the shear strength and shear rate.

(ii) If considering only the influence of K on the shear strength under different shear rates (such as specimens JC09, JC16, JC19, and JC25), the shear strength is shown in Eq. (8).

$$\tau = \left[\sigma_n \tan\left(JRC * \log_{10} K(v_s) + \phi_b\right)\right] * f(v_s)_K, \tag{8}$$

where $f(v_s)_K$ is a function related to the shear strength and shear rate.

(iii) If considering only the influence of σ_n on the shear strength under different shear rates (such as specimens NS09, NS16, NS19, and NS25), the shear strength is shown in Eq. (9).

$$\tau = \left[\sigma_n(v_s) * \tan\left(JRC * \log_{10} K + \phi_b\right)\right] * f(v_s)_{\sigma_n}, \tag{9}$$

where $f(v_s)_{\sigma_n}$ is a function related to the shear strength and shear rate.

To eliminate the effects of JRC, K, and σ_n when obtaining the relationship $f(v_s)_{JRC}$, $f(v_s)_K$, and $f(v_s)_{\sigma_n}$ between the

Table 3 Normalized peak shear stress of the test specimens

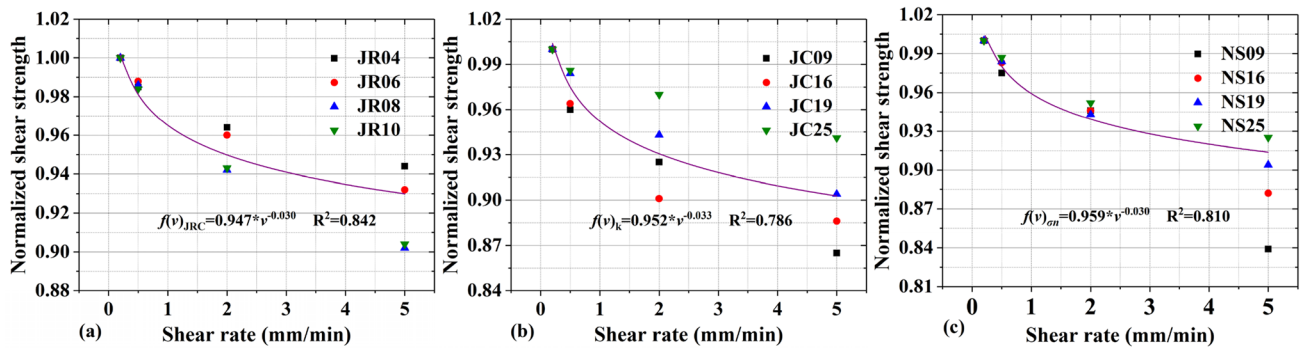| Test group	Normalized peak shear strength			
	0.2 mm/min	0.5 mm/min	2.0 mm/min	5.0 mm/min
JR				
JR04	1.000	0.985	0.964	0.944
JR06	1.000	0.988	0.960	0.932
JR08	1.000	0.986	0.942	0.902
JR10	1.000	0.984	0.943	0.904
JC				
JC09	1.000	0.960	0.925	0.865
JC16	1.000	0.964	0.901	0.886
JC19	1.000	0.984	0.943	0.904
JC25	1.000	0.986	0.970	0.941
NS				
NS09	1.000	0.975	0.946	0.839
NS16	1.000	0.983	0.946	0.882
NS19	1.000	0.984	0.943	0.904
NS25	1.000	0.987	0.952	0.925

Fig. 13 The regression relationship between the normalized peak shear strength and shear rate

shear strength and shear rate, the shear strength collected in this test should be normalized in advance. Compared with the values obtained using a shear rate of 0.2 mm/min, Table 3 demonstrates the normalized shear strength values. Based on the regression analysis between the normalized shear strength and shear rate in Fig. 13, $f(v_s)_{JRC}$, $f(v_s)_K$, and $f(v_s)_{\sigma_n}$ can be concluded as the following equations.

$$f(v_s)_{JRC} = 0.947 * v_s^{-0.030} \qquad R^2 = 0.842, \tag{10}$$

$$f(v_s)_K = 0.952 * v_s^{-0.033} \qquad R^2 = 0.786, \tag{11}$$

$$f(v_s)_{\sigma_n} = 0.959 * v_s^{-0.030} \qquad R^2 = 0.810. \tag{12}$$

By converting Eqs. (7), (8), and (9), $JRC(v_s)$, $K(v_s)$, and $\sigma_n(v_s)$ were calculated with Eqs. (13), (14), and (15). Notably, the value of K is related to the normal stress σ_n; when calculating K with Eq. (13), the valid normal stress $\sigma_n(v_s)$ should be used.

$$JRC(v_s) = \frac{\tan^{-1}\left(\frac{\tau}{\sigma_{n*f(v_s)_{JRC}}}\right) - \phi_b}{\log K}, \tag{13}$$

$$K(v_s) = 10^{\frac{\tan^{-1}\left(\frac{\tau}{\sigma_n(v_s)*f(v_s)_K}\right) - \phi_b}{JRC}}, \tag{14}$$

$$\sigma_n(v_s) = \frac{\tau}{f(v_s)_{\sigma_n} * \tan(\phi_b + JRC * \log K)}. \tag{15}$$

As shown in Fig. 14, the empirical relation between the valid parameters ($JRC(v_s)$, $K(v_s)$, $\sigma_n(v_s)$) and the initial parameters (JRC, K, σ_n) can be proposed through fitting as follows:

$$JRC(v_s) = 5.133 * JRC^{0.555} \qquad R^2 = 0.959, \tag{16}$$

$$K(v_s) = 1.031 * K^{0.999} \qquad R^2 = 0.998, \tag{17}$$

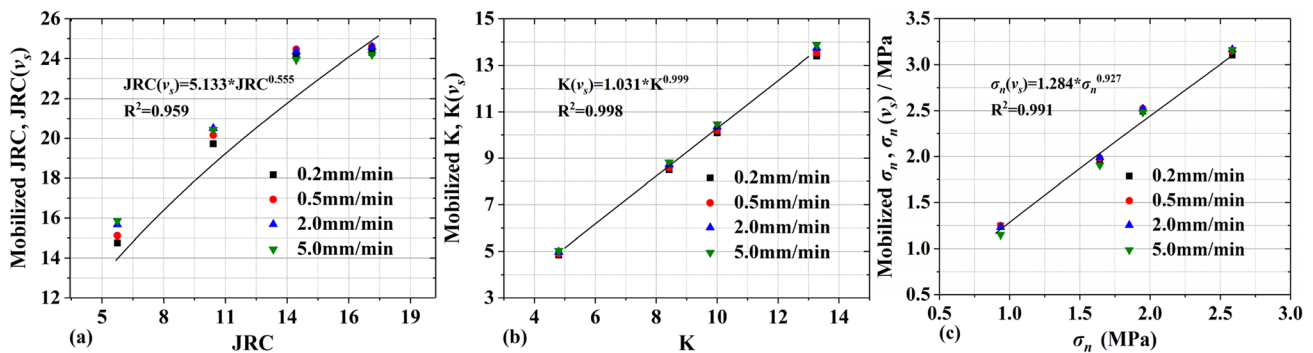$$\sigma_n(v_s) = 1.284 * \sigma_n^{0.927} \qquad R^2 = 0.991. \tag{18}$$

Fig. 14 The relationship between the modified parameters [$JRC(v_s)$, $K(v_s)$, $\sigma_n(v_s)$] and initial parameters (JRC, K, σ_n)
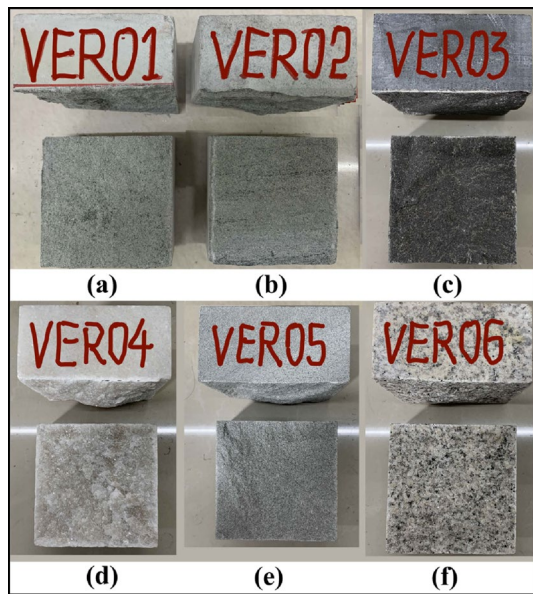
Fig. 15 Split cubic rock joint specimens used for model verification: **a**, **b**, and **e** are sandstone, **c** is limestone, **d** is marble, and **f** is granite

After substituting Eqs. (16), (17), and (18) into Eq. (5), $f(v_s)$ was calculated.

Based on the dimensionless analysis, $\text{JRC}(v_s)$, $\text{K}(v_s)$, and $\sigma_n(v_s)$ were introduced to dimensionless processing for JRC, K, and σ_n. Through multiparameter data fitting, the following equation for the shear rate function can be obtained:

$$f(v_s) = \left[0.0609 * \frac{\text{JRC}(v_s)}{\text{JRC}} - 0.5517 * \frac{\text{K}(v_s)}{\text{K}} + 0.4322 * \frac{\sigma_n(v_s)}{\sigma_n} + 0.6728 \right] * v_s^{(-0.0185)} \quad R^2 = 0.774. \tag{19}$$

Finally, combining Eqs. (5), (16), (17), (18), and (19), it is possible to calculate the shear strength of joints under multiple influencing factors.

5 Verification of the Correlation Model

In this section, direct shear test data under various shear rates on rock joints from the literature are used to verify the proposed correlation model. In addition, natural cubic limestone, sandstone, granite, and marble specimens were subjected to Brazilian splitting tests to generate six rock joint specimens with random asperities on their surfaces for model verification, as shown in Fig. 15. Referring to the calculation method of the 3D JRC value proposed by Grasselli and Egger (2003), the JRC value of the verified specimen is obtained. The other calculated parameters of those joints are listed in Table 4. From the 76 test data points, the JRC value ranges from 3.610 to 17.212, the JCS

value ranges from 9.36 to 41.80 MPa, the shear rate ranges from 0.2 to 24 mm/min, and there are 2D and 3D asperity surface joint specimens. Therefore, the data selected for this verification can represent most rock discontinuity types in nature.

Figure 16 illustrates the calculated versus the measured peak shear strength according to the work of Barton and Wang and this correlation model. Table 4 lists all the calculated results for the peak shear strength. It is concluded that Wang's model and the correlation model work well in predicting the peak shear strength, but the correlation model is slightly better than Wang's model for the following reasons:

(1) As illustrated in Fig. 16, the distribution of measured versus calculated data for the correlation model is closer to the ideal line (measured = calculated) compared to the results obtained by the other two models. The slopes of the fitted lines are 0.815 for Barton's model, 0.865 for Wang's model, and 0.897 for this model.

(2) As listed in Table 4, by comparing the measured with the calculated values, $\tau_{\text{mea}}/\tau_{\text{cal}}$, for the 76 selected test data points, 8, 12, and 56 observed values are best predicted by Barton's model, Wang's model, and the correlation model, respectively. More than 74% of the results can be predicted more accurately by the new correlation model than by the models of Wang and Barton.

(3) Both the new correlation model and Wang's model can capture the shear strength under the shear rate, while Barton's model cannot capture this behavior. Furthermore, the correlation model also evaluates the valid values of JRC, JCS, and σ_n under different shear rates, and the results conform closely to the actual mechanical behavior.

Although the correlation model proposed in this paper outperforms other models in terms of prediction accuracy, more experimental data are needed for future validation. Moreover, similar to previous models, the correlation model still relies on JRC values to characterize the morphological features of rock joint surfaces. Therefore, there are still limitations in the application of 3D morphological rock joints with the proposed correlation model.

Table 4 Comparison of the predictions of the peak shear stress of joint specimens by different models

Data sources	JRC	JCS (MPa)	σ_n (MPa)	v_s (mm/min)	$\tau_{measured}$	Barton's model Equation (2)		Wang's model Equation (3)		Correlation model Eq. (4)		Optimal solution
						$\tau_{calculate}$ (MPa)	$\frac{\tau_{mea}}{\tau_{cal}}$	$\tau_{calculate}$ (MPa)	$\frac{\tau_{mea}}{\tau_{cal}}$	$\tau_{calculate}$ (MPa)	$\frac{\tau_{mea}}{\tau_{cal}}$	
Wang et al. (2016)	3.670	41.80	2.00	0.6	2.547	1.729	1.473	2.257	1.128	2.381	1.070	Correlation model
	3.670	41.80	2.00	1.2	2.380	1.729	1.376	2.165	1.099	2.350	1.013	Correlation model
	3.670	41.80	2.00	6.0	2.174	1.729	1.257	1.966	1.106	2.281	0.953	Correlation model
	3.670	41.80	2.00	12.0	2.041	1.729	1.180	1.886	1.082	2.252	0.906	Wang's model
	3.670	41.80	2.00	24.0	1.653	1.729	0.956	1.809	0.914	2.224	0.743	Barton's model
	11.050	41.80	2.00	0.6	3.352	2.434	1.377	3.050	1.099	3.424	0.979	Correlation model
	11.050	41.80	2.00	1.2	2.864	2.434	1.177	2.925	0.979	3.380	0.847	Wang's model
	11.050	41.80	2.00	6.0	2.632	2.434	1.081	2.656	0.991	3.281	0.802	Wang's model
	11.050	41.80	2.00	12.0	2.507	2.434	1.030	2.547	0.984	3.239	0.774	Wang's model
	11.050	41.80	2.00	24.0	2.184	2.434	0.897	2.444	0.894	3.198	0.683	Barton's model
	15.010	41.80	2.00	0.6	3.864	2.945	1.312	3.462	1.116	4.169	0.927	Correlation model
	15.010	41.80	2.00	1.2	3.779	2.945	1.283	3.321	1.138	4.116	0.918	Correlation model
	15.010	41.80	2.00	6.0	3.555	2.945	1.207	3.015	1.179	3.995	0.890	Correlation model
	15.010	41.80	2.00	12.0	3.469	2.945	1.178	2.892	1.200	3.944	0.879	Correlation model
	15.010	41.80	2.00	24.0	2.935	2.945	0.997	2.774	1.058	3.894	0.754	Barton's model
	3.610	41.80	2.00	0.6	2.679	1.724	1.554	2.249	1.191	2.374	1.129	Correlation model
	3.610	41.80	2.00	1.2	2.525	1.724	1.464	2.157	1.171	2.343	1.077	Correlation model
	3.610	41.80	2.00	6.0	2.458	1.724	1.426	1.959	1.255	2.275	1.081	Correlation model
	3.610	41.80	2.00	12.0	2.283	1.724	1.324	1.879	1.215	2.246	1.017	Correlation model
	3.610	41.80	2.00	24.0	2.244	1.724	1.301	1.802	1.245	2.217	1.012	Correlation model
Liu et al. (2017)	7.036	22.00	1.00	0.5	1.003	0.852	1.176	1.131	0.886	1.296	0.774	Wang's model
	7.036	22.00	1.50	0.5	1.356	1.224	1.109	1.570	0.864	1.681	0.807	Barton's model
	7.036	22.00	2.00	0.5	1.696	1.581	1.073	1.982	0.856	2.024	0.838	Barton's model
	12.941	22.00	1.00	0.5	1.205	1.125	1.071	1.384	0.871	1.699	0.709	Barton's model
	12.941	22.00	1.50	0.5	1.716	1.558	1.101	1.867	0.919	2.094	0.819	Wang's model
	12.941	22.00	2.00	0.5	2.284	1.964	1.163	2.311	0.988	2.440	0.936	Wang's model
Asadizadeh et al. (2018)	10.000	22.97	0.50	0.3	3.020	0.759	3.979	1.115	2.709	1.594	1.895	Correlation model
	12.000	22.97	0.50	0.3	3.020	0.864	3.495	1.237	2.441	1.926	1.568	Correlation model
	4.000	22.97	1.33	0.3	3.210	1.328	2.418	1.789	1.794	1.914	1.677	Correlation model
	6.000	22.97	1.33	0.3	3.210	1.448	2.218	1.961	1.637	2.107	1.523	Correlation model
VER01	8.840	22.20	3.34	0.8	3.420	3.036	1.126	3.504	0.976	3.363	1.017	Correlation model
VER02	12.180	22.20	2.22	3.0	2.750	2.396	1.148	2.547	1.080	2.838	0.969	Correlation model
VER03	6.83	18.6	2.79	1.5	2.769	2.505	0.905	2.817	1.017	2.834	1.023	Wang's model

Table 4 (continued)

Data sources	JRC	JCS (MPa)	σ_n (MPa)	v_s (mm/min)	$\tau_{measured}$	Barton's model Equation (2)		Wang's model Equation (3)		Correlation model Eq. (4)		Optimal solution
						$\tau_{calculate}$ (MPa)	$\frac{\tau_{mea}}{\tau_{cal}}$	$\tau_{calculate}$ (MPa)	$\frac{\tau_{mea}}{\tau_{cal}}$	$\tau_{calculate}$ (MPa)	$\frac{\tau_{mea}}{\tau_{cal}}$	
VER04	14.36	48.3	4.83	2.5	6.032	5.470	0.907	5.709	0.946	5.820	0.965	Correlation model
VER05	10.25	66.1	3.30	3.5	3.633	3.039	0.837	3.438	0.947	3.765	1.036	Correlation model
VER06	7.83	58.5	5.85	4.5	5.303	4.966	0.936	5.380	1.015	5.264	0.993	Correlation model
JR4-020	6.071	19.49	1.95	0.2	2.096	1.582	1.324	2.086	1.004	2.048	1.023	Wang's model
JR4-050	6.071	19.49	1.95	0.5	2.065	1.582	1.305	1.975	1.046	2.013	1.026	Correlation model
JR4-200	6.071	19.49	1.95	2.0	2.020	1.582	1.277	1.817	1.112	1.962	1.029	Correlation model
JR4-500	6.071	19.49	1.95	5.0	1.978	1.582	1.250	1.720	1.150	1.929	1.025	Correlation model
JR6-020	10.270	19.49	1.95	0.2	2.499	1.835	1.362	2.343	1.066	2.335	1.070	Wang's model
JR6-050	10.270	19.49	1.95	0.5	2.470	1.835	1.346	2.218	1.113	2.295	1.076	Correlation model
JR6-200	10.270	19.49	1.95	2.0	2.399	1.835	1.307	2.041	1.175	2.237	1.072	Correlation model
JR6-500	10.270	19.49	1.95	5.0	2.328	1.835	1.269	1.932	1.205	2.200	1.058	Correlation model
JR8-020	13.898	19.49	1.95	0.2	2.940	2.083	1.411	2.543	1.156	2.600	1.131	Correlation model
JR8-050	13.898	19.49	1.95	0.5	2.898	2.083	1.392	2.407	1.204	2.556	1.134	Correlation model
JR8-200	13.898	19.49	1.95	2.0	2.768	2.083	1.329	2.215	1.250	2.492	1.111	Correlation model
JR8-500	13.898	19.49	1.95	5.0	2.652	2.083	1.273	2.097	1.265	2.450	1.083	Correlation model
JR10-020	17.212	19.49	1.95	0.2	2.960	2.340	1.265	2.718	1.089	2.860	1.035	Correlation model
JR10-050	17.212	19.49	1.95	0.5	2.914	2.340	1.245	2.572	1.133	2.812	1.036	Correlation model
JR10-200	17.212	19.49	1.95	2.0	2.792	2.340	1.193	2.367	1.179	2.741	1.019	Correlation model
JR10-500	17.212	19.49	1.95	5.0	2.677	2.340	1.144	2.241	1.195	2.695	0.993	Correlation model
JC9-020	17.212	9.36	1.95	0.2	2.534	1.931	1.312	2.189	1.157	2.133	1.188	Wang's model
JC9-050	17.212	9.36	1.95	0.5	2.432	1.931	1.260	2.072	1.174	2.097	1.160	Correlation model
JC9-200	17.212	9.36	1.95	2.0	2.344	1.931	1.214	1.907	1.229	2.044	1.147	Correlation model
JC9-500	17.212	9.36	1.95	5.0	2.193	1.931	1.136	1.805	1.215	2.010	1.091	Correlation model
JC16-020	17.212	16.42	1.95	0.2	2.949	2.237	1.319	2.582	1.142	2.664	1.107	Correlation model
JC16-050	17.212	16.42	1.95	0.5	2.842	2.237	1.271	2.444	1.163	2.619	1.085	Correlation model
JC16-200	17.212	16.42	1.95	2.0	2.659	2.237	1.189	2.249	1.182	2.553	1.042	Correlation model
JC16-500	17.212	16.42	1.95	5.0	2.612	2.237	1.168	2.129	1.227	2.510	1.041	Correlation model
JC25-020	17.212	25.86	1.95	0.2	3.202	2.524	1.269	2.962	1.081	3.234	0.990	Correlation model
JC25-050	17.212	25.86	1.95	0.5	3.157	2.524	1.251	2.804	1.126	3.180	0.993	Correlation model
JC25-200	17.212	25.86	1.95	2.0	3.106	2.524	1.231	2.580	1.204	3.099	1.002	Correlation model
JC25-500	17.212	25.86	1.95	5.0	3.013	2.524	1.194	2.442	1.234	3.047	0.989	Correlation model
NS09-020	17.212	9.36	0.94	0.2	1.478	1.124	1.315	1.305	1.132	1.508	0.980	Correlation model
NS09-050	17.212	9.36	0.94	0.5	1.441	1.124	1.282	1.235	1.166	1.482	0.972	Correlation model

Table 4 (continued)

| Data sources	JRC	JCS (MPa)	σ_n (MPa)	v_s (mm/min)	$\tau_{measured}$	Barton's model Equation (2) $\tau_{calculate}$ (MPa)	$\frac{\tau_{mea}}{\tau_{cal}}$	Wang's model Equation (3) $\tau_{calculate}$ (MPa)	$\frac{\tau_{mea}}{\tau_{cal}}$	Correlation model Eq. (4) $\tau_{calculate}$ (MPa)	$\frac{\tau_{mea}}{\tau_{cal}}$	Optimal solution
NS09-200	17.212	9.36	0.94	2.0	1.363	1.124	1.213	1.137	1.199	1.445	0.943	Correlation model
NS09-500	17.212	9.36	0.94	5.0	1.240	1.124	1.103	1.076	1.152	1.420	0.873	Barton's model
NS16-020	17.212	16.42	1.64	0.2	2.329	1.972	1.181	2.290	1.017	2.463	0.946	Wang's model
NS16-050	17.212	16.42	1.64	0.5	2.288	1.972	1.160	2.167	1.056	2.421	0.945	Correlation model
NS16-200	17.212	16.42	1.64	2.0	2.204	1.972	1.118	1.994	1.105	2.360	0.934	Correlation model
NS16-500	17.212	16.42	1.64	5.0	2.054	1.972	1.042	1.888	1.088	2.320	0.885	Barton's model
NS25-020	17.212	25.86	2.59	0.2	3.683	3.105	1.186	3.606	1.021	3.662	1.006	Correlation model
NS25-050	17.212	25.86	2.59	0.5	3.634	3.105	1.170	3.413	1.065	3.600	1.009	Correlation model
NS25-200	17.212	25.86	2.59	2.0	3.505	3.105	1.129	3.141	1.116	3.509	0.999	Correlation model
NS25-500	17.212	25.86	2.59	5.0	3.406	3.105	1.097	2.973	1.146	3.450	0.987	Correlation model
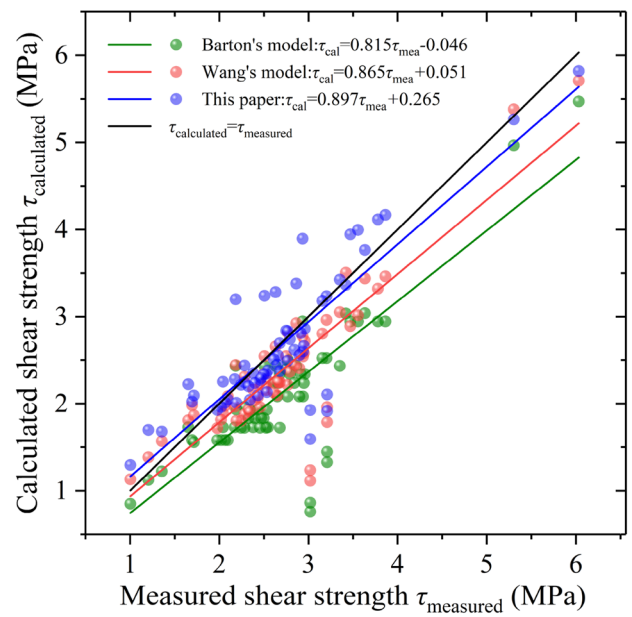
Fig. 16 Comparison of calculated versus measured peak shear strength values from the models of Barton and Wang and this model

6 Conclusions

In this study, direct shear tests were performed on a series of rock joint specimens, and the influence of different shear rates on the joint mechanical behavior and failure modes was investigated for various values of JRC, JCS, and σ_n. The salient conclusions of this study are as follows.

(1) The shear strength versus shear displacement curves show that the shear rate is negatively correlated with the peak shear strength and positively correlated with the peak shear displacement, and the residual shear strength also tends to decrease with the shear rate. The joints with higher JRC and smaller JCS and σ_n show that the peak shear strength and peak shear displacement were more greatly influenced by the shear rate change. Furthermore, the normal displacement versus shear displacement curves demonstrate that the peak normal displacement is enhanced with the shear rate.

(2) Comparing the asperity roughness of the specimens before and after the test shows that with increasing initial JRC, JCS, and σ_n, the JRC degradation ratio is more sensitive to the shear rate. Shear-off and wear are the main failure modes that are observed in these tests. As the shear rate increases, both the shear-off and wear failure areas on the asperity surface increase to a certain extent, but the failure mode of the joint tends to change from wear to shear-off failure. The shear rate dependency of the failure mode change is enhanced when JRC, JCS, and σ_n decrease.

(3) The valid values of JRC, JCS, and σ_n under different shear rates are provided. A new shear strength correlation model that considers the shear rate is proposed through regression fits of test data. All 76 experimental data points taken from the literature and tests are used to validate the performance of the model. Compared with Barton's and Wang's predicted results, the results calculated by the proposed model provide a more accurate estimate of the peak shear strength of rock joints.

Declarations

Conflict of Interest The authors declare that they have no known competing financial interests or personal relationships that could have appeared to influence the work reported in this paper.

References

Amadei B, Saeb S (1990) Constitutive models of rock joints. In: International Symposium on Rock Joints. A.A. Balkema, Leon

Amadei B, Wibowo J, Sture S, Price RH (1998) Applicability of existing models to predict the behavior of replicas of natural fractures of welded tuff under different boundary conditions. Geotech Geol Eng 16(2):79–128

Asadi MS, Rasouli V, Barla G (2012) A bonded particle model simulation of shear strength and asperity degradation for rough rock fractures. Rock Mech Rock Eng 45(5SI):649–675

Asadizadeh M, Moosavi M, Hossaini MF, Masoumi H (2018) Shear strength and cracking process of non-persistent jointed rocks: an extensive experimental investigation. Rock Mech Rock Eng 51(2):415–428

Astm C (2005) 150 standard specification for Portland cement. American Society for Testing and Materials, West Conshohocken

Atapour H, Moosavi M (2014) The influence of shearing velocity on shear behavior of artificial joints. Rock Mech Rock Eng 47(5):1745–1761

Barbero M, Barla G, Zaninetti A (1996) Dynamic shear strength of rock joints subjected to impulse loading. Int J Rock Mech Min Sci Geomech Abstr 33(2):141–151

Barton N, Choubey V (1977) The shear strength of rock joints in theory and practice. Rock Mech 10(1–2):1–54

Crawford AM, Curran JH (1981) The influence of shear velocity on the frictional resistance of rock discontinuities. Int J Rock Mech Min Sci Geomech Abstr 18(6):505–515

Grasselli G, Egger P (2003) Constitutive law for the shear strength of rock joints based on three-dimensional surface parameters. Int J Rock Mech Min Sci (Oxford, England: 1997) 40(1):25–40

Gui Y, Xia C, Ding W, Qian X, Du S (2019) Modelling shear behaviour of joint based on joint surface degradation during shearing. Rock Mech Rock Eng 52(1):107–131

Han G, Jing H, Jiang Y, Liu R, Wu J (2020) Effect of cyclic loading on the shear behaviours of both unfilled and infilled rough rock joints under constant normal stiffness conditions. Rock Mech Rock Eng 53(1):31–57

Hong E, Kwon T, Song K, Cho G (2016) Observation of the degradation characteristics and scale of unevenness on three-dimensional artificial rock joint surfaces subjected to shear. Rock Mech Rock Eng 49(1):3–17

Huang TH, Chang CS, Chao CY (2002) Experimental and mathematical modeling for fracture of rock joint with regular asperities. Eng Fract Mech 69(17):1977–1996

Jafari MK, Amini Hosseini K, Pellet F, Boulon M, Buzzi O (2003) Evaluation of shear strength of rock joints subjected to cyclic loading. Soil Dyn Earthq Eng 23(7):619–630

Jafari MK, Pellet F, Boulon M, Hosseini KA (2004) Experimental study of mechanical behaviour of rock joints under cyclic loading. Rock Mech Rock Eng 37(1):3–23

Jing L (1990) Numerical modeling of jointed rock masses by distinct element method for two and three-dimensional problems. Lulea University of Technology, Lulea

Kou M, Liu X, Tang S, Wang Y (2019) Experimental study of the prepeak cyclic shear mechanical behaviors of artificial rock joints with multiscale asperities. Soil Dyn Earthq Eng 120:58–74

Kulatilake PHSW, Shou G, Huang TH, Morgan RM (1995) New peak shear strength criteria for anisotropic rock joints. Int J Rock Mech Min Sci Geomech Abstracts 32(7):673–697

Ladanyi B, Archambault G (1969) Simulation of the shear behaviour of a jointed rock mass. The 11th Symposium on Rock Mechanics, Berkeley. 105–125

Li HH (2017) Mechanical responses of rock joints with regular asperities under various shear rates investigated by double shear test. J Test Eval 45(2):470–483

Li Y, Sun S, Tang CA (2019) Analytical prediction of the shear behaviour of rock joints with quantified waviness and unevenness through wavelet analysis. Rock Mech Rock Eng 52(10):3645–4365

Liu Q, Tian Y, Liu D, Jiang Y (2017) Updates to JRC-JCS model for estimating the peak shear strength of rock joints based on quantified surface description. Eng Geol 228:282–300

Meng F, Wong LNY, Zhou H, Yu J, Cheng G (2019) Shear rate effects on the post-peak shear behaviour and acoustic emission characteristics of artificially split granite joints. Rock Mech Rock Eng 52(7):2155–2174

Mirzaghorbanali A, Nemcik J, Aziz N (2014) Effects of shear rate on cyclic loading shear behaviour of rock joints under constant normal stiffness conditions. Rock Mech Rock Eng 47(5):1931–1938

Patton (1966) Multiple modes of shear failure in rock. Proc.cong.isrm Lisbon. 282:509–513

Plesha ME (1987) Constitutive models for rock discontinuities with dilatancy and surface degradation. Int J Numer Anal Met 11(4):345–362

Saadat M, Taheri A, Kawamura Y (2021) Incorporating asperity strength into rock joint constitutive model for approximating asperity damage: an insight from DEM modelling. Eng Fract Mech 248:107744

Tang ZC, Wong LNY (2016) New criterion for evaluating the peak shear strength of rock joints under different contact states. Rock Mech Rock Eng 49(4):1191–1199

Tang ZC, Huang RQ, Liu QS, Wong LNY (2015) Effect of contact state on the shear behavior of artificial rock joint. B Eng Geol Environ 75(2):761–769

Tiwari G, Latha GM (2019) Shear velocity-based uncertainty quantification for rock joint shear strength. B Eng Geol Environ 78(8):5937–5949

Tse R, Cruden DM (1979) Estimating joint roughness coefficients. Int J Rock Mech Min Sci Geomech Abstracts 16(5):303–307

Wang ZL, Konietzky H (2009) Modelling of blast-induced fractures in jointed rock masses. Eng Fract Mech 76:1945–1955

Wang G, Zhang X, Jiang Y, Wu X, Wang S (2016) Rate-dependent mechanical behavior of rough rock joints. Int J Rock Mech Min Sci (Oxford, England: 1997) 83:231–240

Wang Z, Gu L, Shen M, Zhang F, Zhang G, Deng S (2020) Influence of shear rate on the shear strength of discontinuities with different joint roughness coefficients. Geotech Test J 43(3):683–700

Wibowo JL (1994) Effect of boundary conditions and surface damage on the shear behavior of rock joints: tests and analytical predictions. University of Colorado at Boulder, Boulder

Xia C, Tang Z, Xiao W, Song Y (2014) New peak shear strength criterion of rock joints based on quantified surface description. Rock Mech Rock Eng 47(2):387–400

Zhao J (1997a) Joint surface matching and shear strength part A: joint matching coefficient (JMC). Int J Rock Mech Min 34(2):173–178

Zhao J (1997b) Joint surface matching and shear strength part B: JRC–JMC shear strength criterion. Int J Rock Mech Min 34(2):179–185

Zhou H, Meng F, Zhang C, Hu D, Lu J, Xu R (2016) Investigation of the acoustic emission characteristics of artificial saw-tooth joints under shearing condition. Acta Geotech 11(4):925–939